IOP Publishing Measurement Science and Technology
Meas. Sci. Technol. 31 (2020) 054001 (14pp) https://doi.org/10.1088/1361-6501/ab64ad

Comparison of momentum and impulse formulations for PIV-based force estimation

Eric Limacher[1], Jeffrey McClure[2], Serhiy Yarusevych[2] and Chris Morton[3]

[1] Federal University of Pará, Mechanical Engineering, Belém, Brazil
[2] University of Waterloo, Mechanical and Mechatronics Engineering, Waterloo, Canada
[3] University of Calgary, Mechanical and Manufacturing Engineering, Calgary, Canada

E-mail: chris.morton@ucalgary.ca

Received 31 October 2019, revised 15 December 2019
Accepted for publication 20 December 2019
Published 31 January 2020

Abstract

The estimation of fluid-induced loads using particle image velocimetry (PIV) data is investigated using momentum- and impulse-based control volume methods, which require additional calculations of pressure and vorticity surrounding the immersed body, respectively. A new, comprehensive comparison of the two methods is presented based on two-dimensional velocity data. The effects of random error, finite spatio-temporal resolution, and spatial filtering of the velocity fields are considered using numerical (CFD) data of flow around a stationary circular cylinder in a steady freestream at a Reynolds number of $\mathrm{Re} = 150$. In general, the momentum method is found to be more robust, exhibiting lower random-error sensitivity and lower errors due to discretization, except at coarse spatial resolutions, for which a significant underestimation of drag arises using the momentum method. The impulse method is best suited to cases where vorticity does not leave the control volume, or in cases where a deforming control volume can be defined to minimize the presence vorticity on the outer control surface. For example, the impulse method performed as well as the momentum method when applied to particle image velocimetry (PIV) data obtained around a cylinder accelerating from rest in quiescent fluid (with a peak Reynolds number of 5100). For the broad class of flows involving a steady freestream and an established wake, the momentum method can be applied with greater confidence than the impulse method.

Keywords: PIV, force estimation, impulse, pressure calculation

(Some figures may appear in colour only in the online journal)

1. Introduction

As particle image velocimetry (PIV) data have become widely available, the prospect of using these data to estimate force has attracted a great deal of research attention, e.g. Noca *et al* (1999), Van Oudheusden *et al* (2006), David *et al* (2009), Mohebbian and Rival (2012) and Limacher *et al* (2019b). Such estimates could be of great use in applications where direct force measurement is difficult due to the intrusiveness of available measurement techniques, e.g. force transducers or strain gauges, or where it is simply impossible due to the kinematic or geometric complexity of the problem.

Methods of force estimation using PIV data can be organized into two broad categories: momentum methods and impulse methods (Rival and van Oudheusden 2017). In both methods, PIV data are acquired in a two or three-dimensional region surrounding the body of interest. Momentum methods require pressure information to be explicitly evaluated, while impulse methods require the evaluation of vorticity. As pointed out by Rival and van Oudheusden (2017), some of the persistent challenges in obtaining reliable force estimates include how near-body PIV data are treated, how pressure is estimated, effects of temporal and spatial resolutions, etc. In the present work, both momentum and impulse methods are

compared in their ability to accurately extract force estimates from two-dimensional velocity field data, using both numerical data and a PIV dataset.

The conservation of momentum for a stationary, non-deforming control volume (CV) encompassing a stationary body leads to the following well-known equation for the fluid force:

$$\mathbf{F} = -\frac{\mathrm{d}}{\mathrm{d}t}\left(\int_V \rho \mathbf{u}\mathrm{d}V\right) - \int_S \rho\mathbf{u}(\mathbf{u}\cdot\hat{\mathbf{n}})\mathrm{d}S - \int_S p\hat{\mathbf{n}}\mathrm{d}S + \int_S (\boldsymbol{\tau}\cdot\hat{\mathbf{n}})\mathrm{d}S, \tag{1}$$

where V is the fluid volume, S is the outer boundary of V, $\hat{\mathbf{n}}$ is the outward-facing normal on S, $\boldsymbol{\tau}$ is the viscous stress tensor, $\mathbf{F}$ is the instantaneous fluid force acting on the cylinder, $\mathbf{u}$ is the velocity, ρ is the fluid density, and p is the pressure. Details on the implementation of planar momentum balance in three-dimensional flows can be found in McClure and Yarusevych (2019).

For a two-dimensional stationary body in a stationary, non-deforming CV, the impulse formulation (Noca 1997, Kang *et al* 2017) can be expressed as

$$\mathbf{F} = -\rho\frac{\mathrm{d}}{\mathrm{d}t}\int_V \mathbf{x}\times\boldsymbol{\omega}\mathrm{d}V - \rho\oint_S (\hat{\mathbf{n}}\cdot\mathbf{u})(\mathbf{x}\times\boldsymbol{\omega})\mathrm{d}S + \rho\oint_S \left(\frac{1}{2}\hat{\mathbf{n}}u^2 - (\hat{\mathbf{n}}\cdot\mathbf{u})\mathbf{u}\right)\mathrm{d}S + \mu\oint_S \left(\mathbf{x}\times\frac{\partial\boldsymbol{\omega}}{\partial n} - \hat{\mathbf{n}}\times\boldsymbol{\omega}\right)\mathrm{d}S, \tag{2}$$

where $\mathbf{x}$ is the position vector, and $\boldsymbol{\omega}$ is the vorticity. In the present work, the origin will be taken to lie at the centre of the body. The first term on the right-hand side is the rate of change of vortical impulse within the domain, and the second term is the net flux of impulse out from the domain, jointly representing the material derivative of impulse in V. The remaining two integrals jointly account for the material derivative of impulse in the unobserved domain external to V. Hereafter, the four integral terms on the right-hand side of equation (2) will be referred to as the impulse derivative term (or simply the impulse term), the impulse flux term, the velocity term, and the viscous term, respectively. Equation (2) is taken from equations (3.55) and (3.56) of Noca (1997), but with the viscous term expressed in the more convenient form given by Kang *et al* (2017).

In the present study, discretized versions of the momentum and impulse force formulations are applied to two test cases: (i) data from a numerical simulation of the flow around a two-dimensional circular cylinder (of diameter D) in a steady freestream (U_∞) at a Reynolds number of 150, and (ii) data from a PIV experiment of an accelerating cylinder in quiescent fluid at a peak Reynolds number of approximately 5100 (Limacher *et al* 2019b). The first test case was considered to facilitate a comparative analysis of the sensitivity of the two methods to random errors and to spatio-temporal resolutions representative of PIV data. These same considerations have been studied for the momentum method alone by David *et al* (2009). The key contribution of the present work is the direct comparison of momentum- and impulse-based approaches on the same datasets. In order to mimic PIV datasets, the numerical solution was interpolated onto a square Cartesian grid. To analyze random-error sensitivity, synthetically generated random errors are added to the velocity fields prior to the calculation of force. The second test case provides an experimental comparison basis using a different flow scenario, demonstrating the feasibility of both methods under specific conditions. Details on the discretization of equations (1) and (2) are given in section 2, while the numerical and experimental results are presented in sections 3 and 4, respectively.

2. Discretization of momentum and impulse equations

For the impulse formulation, second-order central difference schemes are used for spatial and temporal derivatives. For both methods, trapezoidal integration along each segment of the contour S is employed, and midpoint integration is employed for the area integral. In the impulse method, to avoid overestimating the contribution of data points adjacent to the contour S, the contour is defined to lie halfway between the grid points used in the area integral. Data points on the contour are then linearly interpolated from the adjacent grid points. In the momentum formulation, the outer control surface is chosen to lie on grid points, and the contribution to the area integral by the boundary points is truncated instead. The influence of the contour definition on the final solution is expected to be minor when spatial discretization is sufficiently fine to resolve gradients in the field at the boundary.

For the momentum formulations, the pressure field is estimated from the discretized velocity field and its derivatives by solving the Poisson equation using an Eulerian approach (de Kat and van Oudheusden 2012) with boundary conditions and source terms computed from the PIV data (van Oudheusden 2013). Since different boundary conditions exhibit different sensitivities to experimental error (Pan *et al* 2016), two versions will be compared herein: the Neumann case, where Neumann boundary conditions are employed on all the cylinder and domain boundaries, and the Dirichlet case, where Neumann conditions are employed on the cylinder, upstream and downstream boundary conditions, and Dirichlet boundary conditions are employed on the top and bottom domain boundaries. For the Dirichlet condition, the pressure on the boundary is set using an extended form of the Bernoulli equation, valid for unsteady, irrotational flow with small mean velocity gradients (de Kat and van Oudheusden 2012). The Laplacian of the pressure field is discretized using a five-point second-order central difference scheme, which entails the use of 'ghost grid points' at the boundaries (McClure and Yarusevych 2017a).

As will be demonstrated later, errors in the impulse-based force estimates are exacerbated by the presence of vorticity on the outer control surface. As a result, two versions of the impulse formulation are presented: one with a static CV, and one with a dynamic CV wherein the downstream plane location, x_D, is selected at each instant in time to minimize the integral of enstrophy on S. Since equation (2) is valid only for a static CV, the force at each instant for the dynamic CV method must be calculated from a series of three data points

Table 1. Control volume definitions for various methods. The location of the downstream face, $x_D^* \in [5, 9]$, varies in the dynamic CV definition so as to minimize the integral of enstrophy on S. h^* is the spatial resolution of the discrete field data (normalized by cylinder diameter).

Methodology	CV definition: $[x^*_{\min}, x^*_{\max}, y^*_{\min}, y^*_{\max}]$
Momentum, Dirichlet BC:	$[-1,\ 1,\ -1,\ 1]$
Momentum, Neumann BC:	$[-1,\ 1,\ -1,\ 1]$
Impulse, static CV:	$[-1,\ 5,\ -2.4,\ 2.4] + 0.5h^*[-1,\ 1,\ -1,\ 1]$
Impulse, dynamic CV:	$[-1,\ x_D^*,\ -2.4,\ 2.4] + 0.5h^*[-1,\ 0,\ -1,\ 1]$

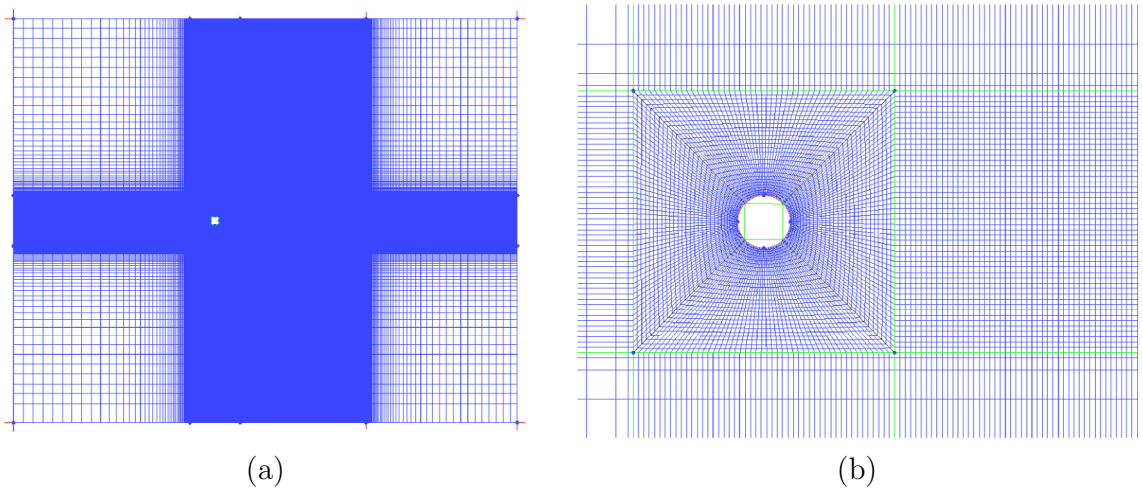

Figure 1. Grid used for the simulation: (a) full domain, showing only every second node for clarity; (b) immediate vicinity of the cylinder, showing the O-grid and the surrounding rectangular grid blocks (showing only every tenth node).

to permit the approximation of the time derivative of impulse by central differencing. For the numerical data, the domain of possible downstream plane locations is $x_D^* = x_D/D \in [5, 9]$, where D is the cylinder diameter. The downstream extent of this domain, though likely inconvenient to resolve in PIV investigations, is employed here to demonstrate the possibility of error reduction. The control volumes employed for the different methodologies are listed in table 1, expressed in terms of the normalized coordinates $x^* = x/D$ and $y^* = y/D$, with the origin at the centre of the cylinder. Likewise, the distance between grid points of the discrete dataset, h, is normalized as $h^* = h/D$.

3. Numerical investigation

3.1. CFD methodology

A solver from Fluent 15.0 was used to compute the unsteady, incompressible flow around a two-dimensional circular cylinder at a Reynolds number of $\mathrm{Re} = \rho U_\infty D/\mu = 150$. A finite-volume approach was used, employing the SIMPLE algorithm (Versteeg and Malalasekera 2007) to solve the continuity and Navier–Stokes equations. The employed spatial discretization schemes are as follows: least-squares cell-based for gradient, second-order for pressure, and second-order upwind for momentum. Temporal discretization was achieved using a second-order implicit transient scheme. A constant velocity boundary condition was specified on the upstream face, and an outflow boundary condition was specified on the downstream plane. The no-slip and impermeable boundaries were imposed at the cylinder surface, and the lateral outer domain boundaries were specified as impermeable but with zero shear.

The grid featured an O-grid block centred on the cylinder surrounded by rectangular grid blocks. A sample image of the computational domain and grid is shown in figure 1. The calculation domain extended 20 diameters upstream, 30 diameters downstream, and 20 diameters to either side of the cylinder. For $-2.5 < x^* < 12.5$ and $-2.5 < y^* < 2.5$, the nominal grid spacing is $h = 0.01$D. This refinement in the wake was necessary to prevent numerical diffusion that would artificially decrease the calculated magnitude of the vortical impulse. Outside of this region, the grid coarsens towards the boundaries, with the cell aspect ratio growing to a maximum of 20 at the boundaries. Adjacent to the cylinder, the radial spacing of the grid is further refined to $0.005D$, yielding a maximum value of $y^+_{\max} = 0.322$ at the cylinder surface. The resulting computational grid is over 1.7 million nodes, and a constant time step of $\Delta t = 0.005$s was used.

The solution was initialized by interpolating a transient solution from a coarser grid onto the finer grid described above. The coarse grid simulation was run until the formation of a stable and symmetric vortex street was observed. After interpolation to the finer grid, the simulation was run until the mean drag and root-mean-square (RMS) lift coefficients had reached an acceptable level of convergence, as demonstrated in figure 2 for $t^* = tU_\infty/D \geqslant 0$.

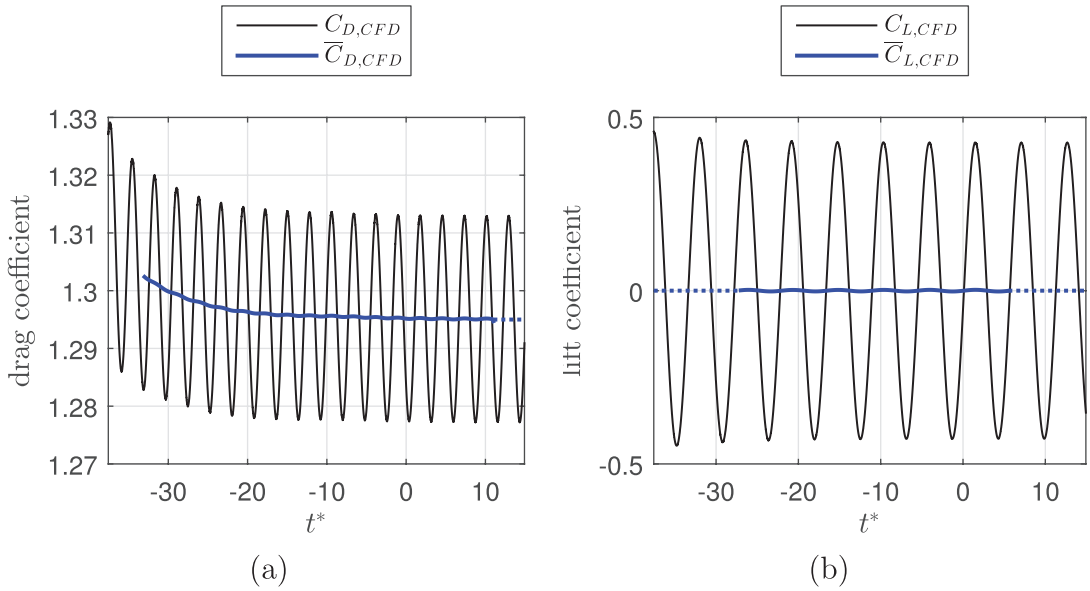

Figure 2. Instantaneous force coefficients, $C_{D,\mathrm{CFD}}$ and $C_{L,\mathrm{CFD}}$, calculated directly from surface stresses on the cylinder (black lines) versus dimensionless time, t^*: (a) drag coefficient; (b) lift coefficient. The blue lines give the moving averages, $\overline{C}_{D,\mathrm{CFD}}$ and $\overline{C}_{D,\mathrm{CFD}}$, over one-half of a shedding period for the drag, and one full shedding period for the lift. The dashed blue lines are extensions of these moving averages within one averaging window from the ends of the signal.

Table 2. Strouhal number, RMS lift coefficient, and mean drag coefficient for the present simulation, alongside numerical and experimental results from the literature. All values apart from the present work have been copied directly from table 1 of McClure *et al* (2015).

Study	Type	St	$C_{L,\mathrm{RMS}}$	$\overline{C_D}$
Present results	Numerical	0.178	0.303	1.30
McClure *et al* (2015)	Numerical	0.185	0.366	1.33
Morton and Yarusevych (2010)	Numerical	0.190	...	1.35
Marzouk *et al* (2007)	Numerical	0.179	0.349	1.31
Norberg (2003)	Experimental	0.183	0.356	...
Henderson (1995)	Numerical	...	...	1.36
Wieselberger (1921)	Experimental	...	...	1.30

Table 3. Parameter space of spatial and temporal resolutions investigated using the CFD results.

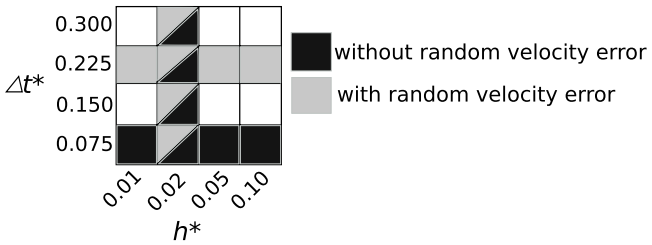

The present simulation yielded a mean drag coefficient of $\overline{C_D} = 1.295$, a Strouhal number of $St = fD/U_\infty = 0.178$, and an RMS lift coefficient of $C_{L,\mathrm{RMS}} = 0.303$. These results are in good agreement with other numerical simulations (Henderson 1995, Marzouk *et al* 2007, Morton and Yarusevych 2010, McClure *et al* 2015) and experiments (Norberg 2003, Wieselberger 1921) of the flow around nominally two-dimensional circular cylinders at a Reynolds number of $\mathrm{Re} = 150$, as summarized in table 2. Apart from the present results, all values in table 2 are taken directly from table 1 of McClure *et al* (2015), being reproduced here for ease of reference.

3.2. Synthetic PIV error and parameter space

The numerical solution data were interpolated onto a square Cartesian grid of $h^* = h/D = 0.01$ with a dimensionless time separation of $\Delta t^* = \Delta t D/U_\infty = 0.075$ between consecutive fields. Spatial and temporal resolutions were then varied by under-sampling the data from the interpolated grid (table 3), spanning $0.01 < h^* < 0.1$ in space and $0.075 < \Delta t^* < 0.3$ in time.

To quantify the sensitivity of the force estimations to random measurement errors, synthetic random errors were added to the sampled velocity fields representative of those typically encountered in PIV experiments. Figure 3(a) shows a single instantaneous realization of the generated streamwise velocity error for a spatial resolution of $h^* = 0.02$, and figure 3(b) shows the corresponding instantaneous normalized vorticity field, $\omega^* = \omega D/U_\infty$, with the generated errors. The standard deviation, (σ) of the error at a given spatial location and time is prescribed using the two-parameter model of McClure and Yarusevych (2017b), expressed as

$$\sigma = U_{\max}\left[\sigma_{\mathrm{global}} + \sigma_{\mathrm{flow}}\frac{|\nabla \mathbf{u}|}{\max(|\nabla \mathbf{u}|)}\right]. \qquad (3)$$

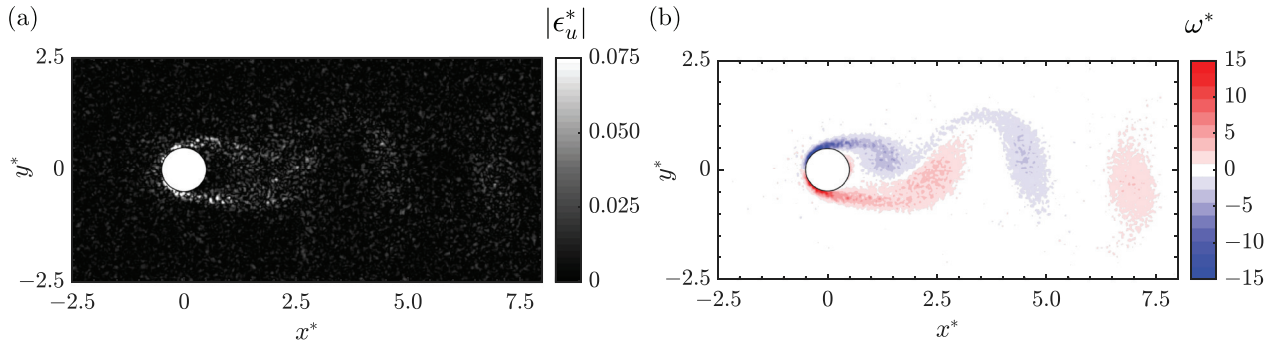

Figure 3. Example of the synthetic random error applied to the sampled cylinder flow velocity data: (a) instantaneous magnitude of the streamwise velocity error, (b) instantaneous vorticity field with errors.

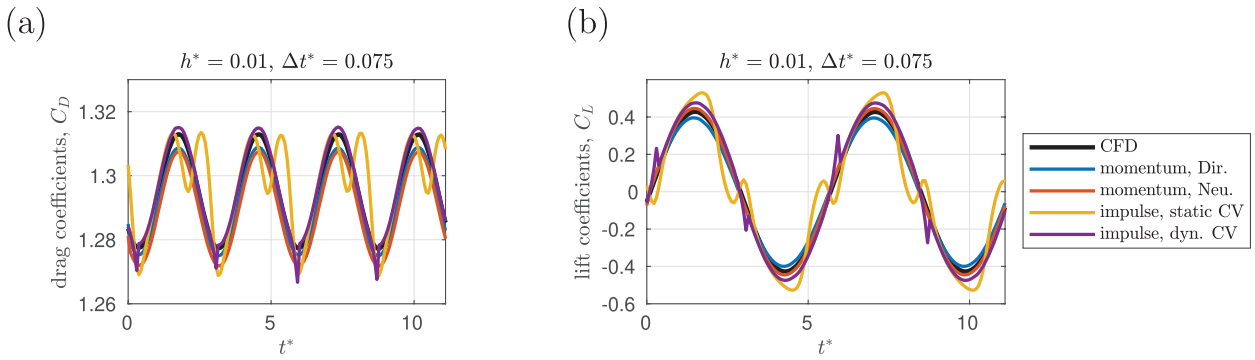

Figure 4. Force coefficients for the finest resolution case $h^* = 0.01$, $\Delta t^* = 0.075$: (a) drag coefficients; (b) lift coefficients.

The first term specifies a global source of error, uniform across the domain, and the second term lends errors proportional to the local magnitude of the velocity gradient tensor. In the present work, except where otherwise stated, $\sigma_{\text{global}} = 0.5\%$ and $\sigma_{\text{flow}} = 7.5\%$. The prescription of a constant σ_{flow}, rather than the more general relation of McClure and Yarusevych (2017b) involving the spatial and temporal resolutions of PIV acquisition, is justified if we presume the experimentalist varies the laser pulse separation for each case to maintain a constant interframe particle displacement in the freestream. The selected 0.5% error corresponds to a 0.06 px peak detection error when the maximum particle displacement is half of a 24×24 px interrogation window. This places a lower bound on the time separations in which the constant free-stream error assumption is valid, since the time separation between vector fields cannot be less than the pulse separation. Hence, random-error sensitivity of the force estimation methods is only studied for cases where $\Delta t^*/4h^* > 0.5$ (see table 3). To model the spatial correlation of PIV errors due to an interrogation window overlap of 75% (Sciacchitano and Wieneke 2016), the uncorrelated random error field generated at each instant is convolved with a 7×7 matrix that results in a positive autocorrelation of the errors, decreasing linearly with spatial separation for spatial separations less than one interrogation window width.

3.3. Force estimates from numerical data

Force coefficient estimates with the subscripts *mom* and *imp* to refer to the momentum and impulse formulations. The additional subscripts *Neu* and *Dir* denote the two alternative boundary conditions used in the momentum method, and the additional subscript *dyn* refers to the variation of the impulse method in which the CV is varied in time to minimize enstrophy on S. The subscript *CFD* refers to force coefficients obtained directly by integration of the stresses on the cylinder. The instantaneous lift and drag are normalized by $1/2\rho DU_\infty^2$ to yield lift and drag coefficients C_L and C_D, respectively.

Figure 4 plots the results of each of the force estimation methods for the finest spatial and temporal resolutions available, that is, $h^* = 0.01$ and $\Delta t^* = 0.075$, without random error added to the velocity fields. The impulse method with a static CV exhibits periodic errors in both lift and drag relative to the CFD results. The occurrences of greatest instantaneous error are correlated with vortices crossing the contour S. Using a dynamic CV, with a downstream face situated between vortices and advancing with the wake, instantaneous errors are greatly reduced. The remaining erroneous spikes in $C_{D,\text{imp,dyn}}$ and $C_{L,\text{imp,dyn}}$ occur when the downstream face (containing the lowest enstrophy) reaches the limits of the permissible domain and then discontinuously jumps to an upstream spatial location. The momentum method exhibits low error in lift and drag, with a minor bias error in drag estimates. Given the use of a Neumann boundary condition on the downstream wake plane, the momentum method is not affected by the presence of vorticity on the outer contour.

Root-mean-square (RMS) errors in the drag and lift coefficients, ϵ_D^{RMS} and ϵ_L^{RMS}, are calculated over two complete shedding cycles. Figure 5 shows the RMS errors for each

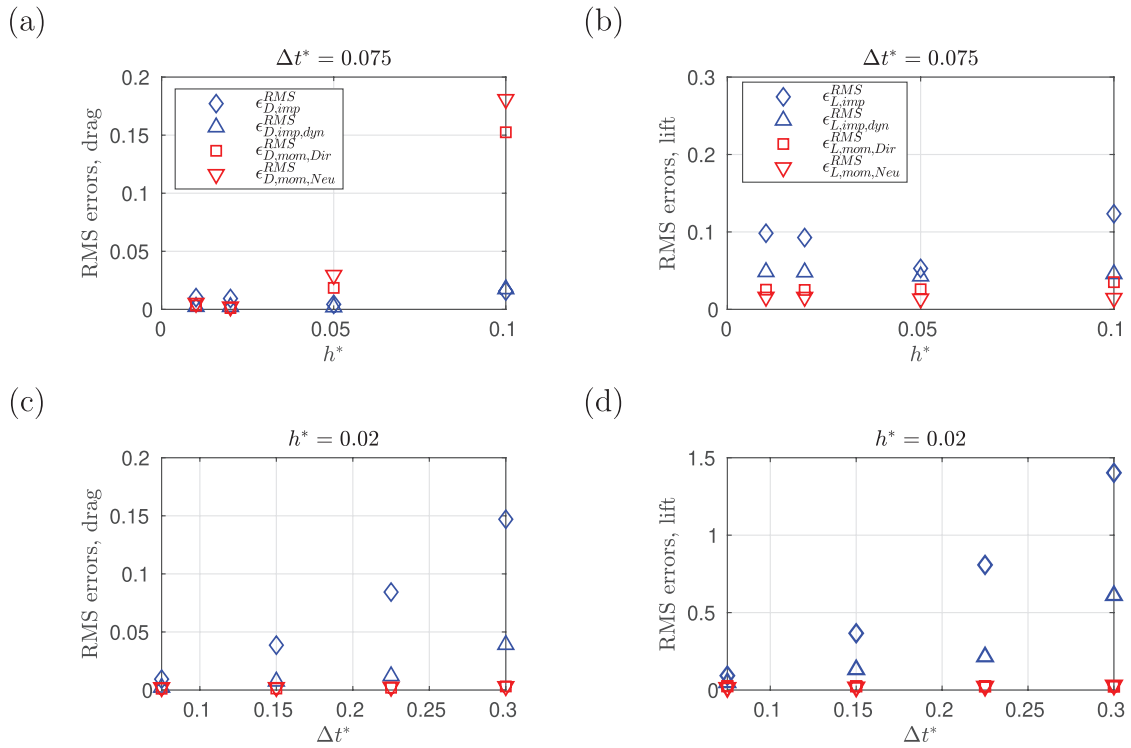

Figure 5. RMS errors for each of the force estimation methods for varied temporal and spatial resolutions. (a) and (b) constant temporal resolution $\Delta t^* = 0.075$, varied spatial resolution; (c) and (d) constant spatial resolution $h^* = 0.02$, varied temporal resolution. Drag coefficients are on the left, lift coefficients are on the right.

method, identified by the earlier defined subscripts, for the combinations of spatial and temporal resolutions studied. The momentum method yields lower RMS errors than the impulse method for all cases other than for drag at coarse spatial resolutions, i.e. $h^* \geqslant 0.05$ (figure 5(a). For the impulse method, the use of a dynamic CV reduces the RMS errors to levels similar to the momentum method, except for the two coarsest temporal resolutions where more pronounced deviations are observed in the lift data (figure 5(d)).

The impulse method exhibits minima in the RMS error for both drag and lift at a spatial resolution of $h^* = 0.05$ in figures 5(a) and (b). This minimum can be explained by the interaction between the impulse-derivative and impulse-flux terms (the first two terms on the right-hand side of equation (2)), the sum of which represents the material derivative of impulse in V, as presented in figures 6(a) and (b). Small relative errors in the impulse-derivative or impulse flux terms lead to errors of significant relative magnitude in their sum. With increasing h^*, calculated vorticity values decrease, reducing the value of both of these terms, and thus also the relative error in their sum. This reduction can result in a net decrease in error for moderate increases in h^*, but will eventually yield to increasing errors as the calculated vorticity becomes increasingly inaccurate. The drag and lift contributions of the material derivative of impulse are compared to the contributions from the velocity term and the viscous term in figures 6(c) and (d). The out-of-phase behaviour of the impulse material derivative and the velocity term is unsurprising, given that the velocity term can be equivalently expressed as an area integral of the Lamb vector, $\mathbf{u} \times \boldsymbol{\omega}$ (Wu *et al* 2015). The non-negligible contribution of the viscous term to the lift force is due to the long moment arm between the origin and the downstream plane in the $\mathbf{x} \times \partial\omega/\partial n$ term.

Figure 7 presents the calculated lift and drag coefficients, without random error added to the velocity fields, at varied spatial resolution at a constant temporal resolution of $\Delta t^* = 0.075$. The errors for the static-CV impulse method are of near-zero mean, but are not negligible instantaneously (see figures 7(a) and (b)). The use of a dynamic CV significantly reduces the instantaneous errors, leaving minor erroneous spikes where the CV discontinuously jumps upstream (figures 7(c) and (d)). A bias in the drag coefficients for the momentum method, which grows as the spatial resolution coarsens (figure 7(e)), is found to be the cause of the higher RMS errors seen in figure 5(a); however, the lift estimates are not affected significantly by increasing h^* (figure 7(f)). The results using the Dirchlet and Neumann boundary conditions are nearly identical, so the latter has been omitted from figure 7 for brevity.

The impulse method is highly sensitive to the coarsening of the temporal resolution (figures 5(c) and (d)). As Δt^* increases, the vortical structures in the wake travel an increasing fraction of a cylinder diameter between vector fields, increasing truncation error in the approximated time derivative of impulse. Contrary to the fine temporal resolution cases, the dynamic CV method fails to bring the errors down to a similar magnitude as the momentum method for the greater Δt^* cases. In contrast, the two momentum method variants both agree with the CFD forces very well and exhibit only minor variation for the range of temporal resolutions considered here.

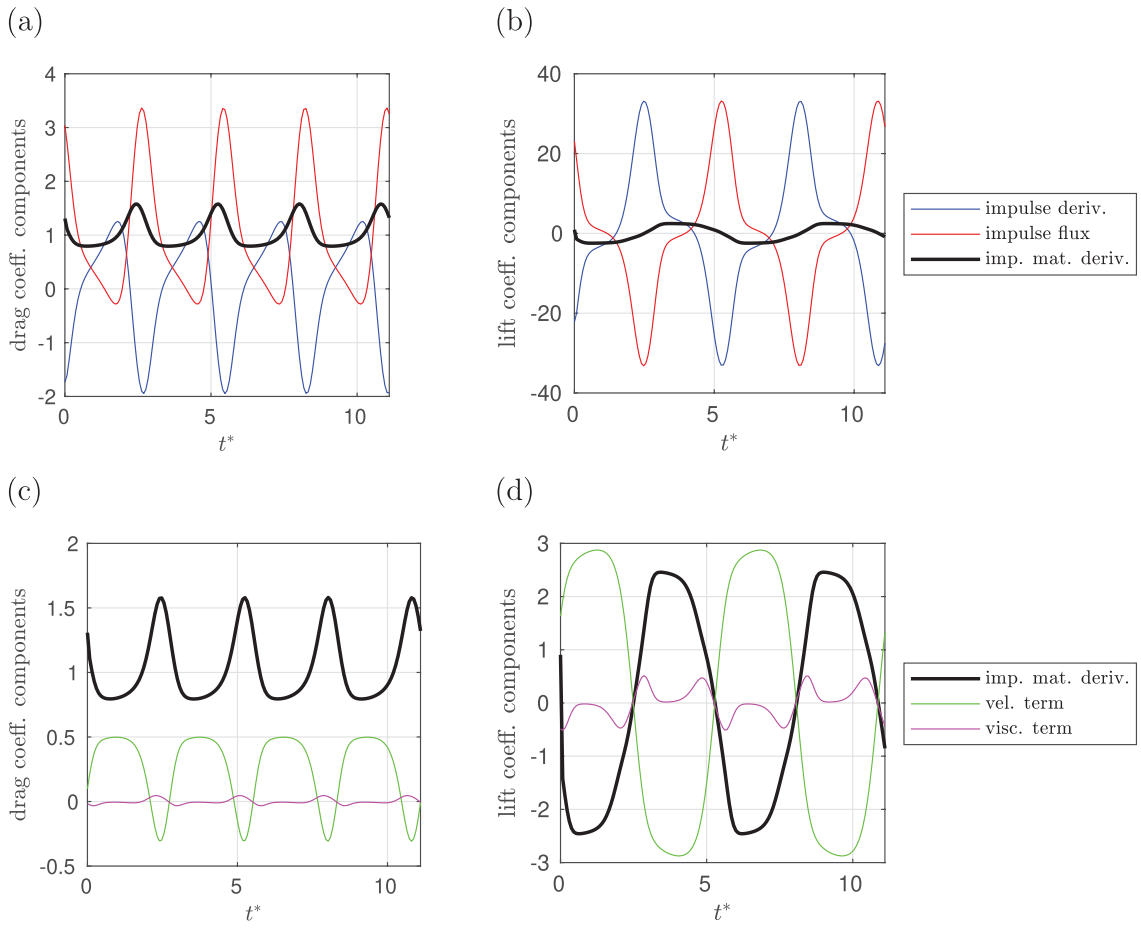

Figure 6. (a) and (b): The impulse derivative (blue line) and impulse flux (red line) terms exhibit large instantaneous contributions to drag and lift, but they sum to a relatively smaller signal (black line), representing the material derivative of impulse in the domain V. (c) and (d): Drag and lift contributions of the impulse material derivative (black line), the velocity term (green line) and the viscous term (magenta line).

The level of temporal resolution needed for adequate application of the impulse method requires a Δt that is at least an order of magnitude smaller than the convective time scale of the flow of interest, i.e. D/U_∞ in the present case. In the present results, RMS errors below 0.05 in both lift and drag coefficient were achieved using the dynamic-CV method only when Δt^* was reduced to 0.075, but similarly low errors were not achieved for any spatiotemporal resolution using the static-CV method, suggesting that greater temporal resolution is required to resolve the contributions due to vorticity flux across the control surface.

3.4. Force estimates from numerical data with correlated random error added to velocity fields

For the case of $h^* = 0.02$ and $\Delta t^* = 0.075$, figure 8 shows the estimated forces for the momentum method and the static-CV impulse method after correlated random error has been added to the velocity fields. The instantaneous error for the impulse method is consistently an order of magnitude greater than the momentum method. The errors are manifested in high-frequency content, suggesting that the time derivative in the first term of equation (2) has amplified the random error due to the presence of a small Δt^* in the denominator of the central difference derivative approximation. Since these errors remain of near-zero mean, it is plausible that they could be filtered in cases with sufficient temporal resolution. Filtering, smoothing, or replacing the evaluated integral $\int_V \mathbf{x} \times \boldsymbol{\omega} \mathrm{d}V$ with a fitted polynomial prior to time differentiation, as done by Lin and Rockwell (1996), would reduce the random error in the resulting force estimates. This has not been considered here, however, since random error propagation through the remaining terms of the impulse equation remains significant, as will be discussed in section 3.5.

Figure 9 shows the RMS errors in drag and lift coefficients for the momentum and impulse methods after adding random error to the velocity fields. In these plots, RMS error is defined with respect to the previously obtained force estimates, indicating how error is increased by the presence of random velocity error rather than reporting total absolute error relative to the CFD results. RMS errors and force coefficients defined in this way are denoted by the tilde symbol, e.g. $\tilde{\epsilon}^{\mathrm{RMS}}_{D,\mathrm{imp}}$. Both variants of the momentum method show minor sensitivity to changes in temporal resolution, with only a slight decrease in error with increasing Δt^*. When h^* is varied in figures 9(a) and (b), the minima at $h^* = 0.02$ suggest that random error propagation through the momentum force formulation

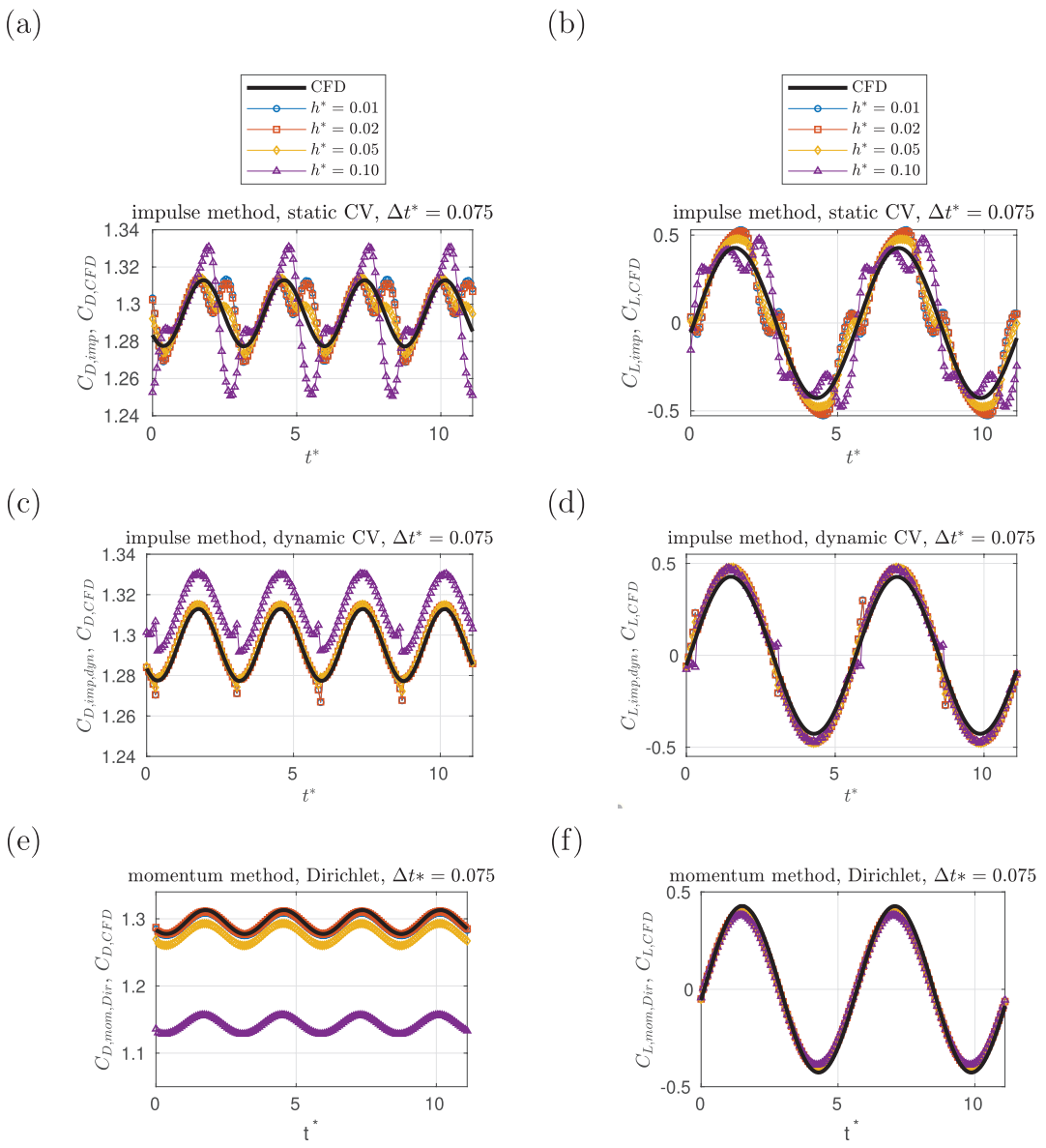

Figure 7. Effect of spatial resolution on force estimates for the various methods at a fixed temporal resolution of $\Delta t^* = 0.075$. (a) and (b): Impulse method for a static CV; (c) and (d) impulse method for a dynamic CV; (e) and (f) momentum method with Dirchlet BC.

becomes more significant as h^* decreases. On the other hand, truncation error propagation through the force formulation is dominant for $h^* \geqslant 0.05$. The impulse method exhibits a minimum in RMS error with respect to both spatial and temporal resolutions (figures 9(a)–(d)). As noted in the discussion of figure 5, the minima with respect to h^* in figures 9(a) and (b) can be explained in terms of reduced error in the sum of the impulse-derivative and impulse-flux terms. The minima with respect to Δt^* in figures 9(c) and (d) can be explained by two competing factors; the amplification of random error through the impulse time derivative decreases as Δt^* increases, but the presence of erroneous vorticity on the outer contour increasingly exacerbates error in the sum of the impulse-derivative and impulse-flux terms as Δt^* increases.

A similar random-error sensitivity analysis for the dynamic-CV impulse method has not been conducted. To provide a best-case representation of the random-error sensitivity of the dynamic CV method, it is advisable to undertake this analysis in conjunction with a more sophisticated method of deformable CV definition than that used herein, such as a method that identifies material curves. Nonetheless, we may estimate the best-case improvement in random-error sensitivity that may be achieved by a dynamic-CV approach by considering the random error propagation through each of the terms in the impulse formulation. This analysis is presented in section 3.5.

3.5. Extended random error analysis for the static-CV impulse method

Random error does not propagate equally through each term in the impulse formulation. The RMS error of each term, as calculated using the velocity fields with error added, are

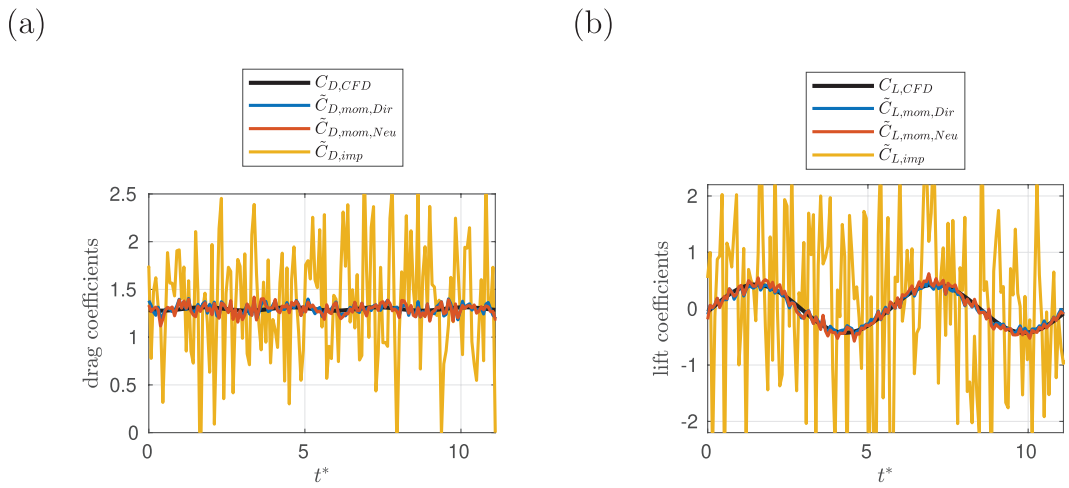

Figure 8. Comparison of momentum and impulse based force estimates for $h^* = 0.02$ and $\Delta t^* = 0.075$ with correlated random error added to the velocity fields: (a) drag coefficients, $\tilde{C}_{D,(\cdot)}$; (b) lift coefficients, $\tilde{C}_{L,(\cdot)}$.

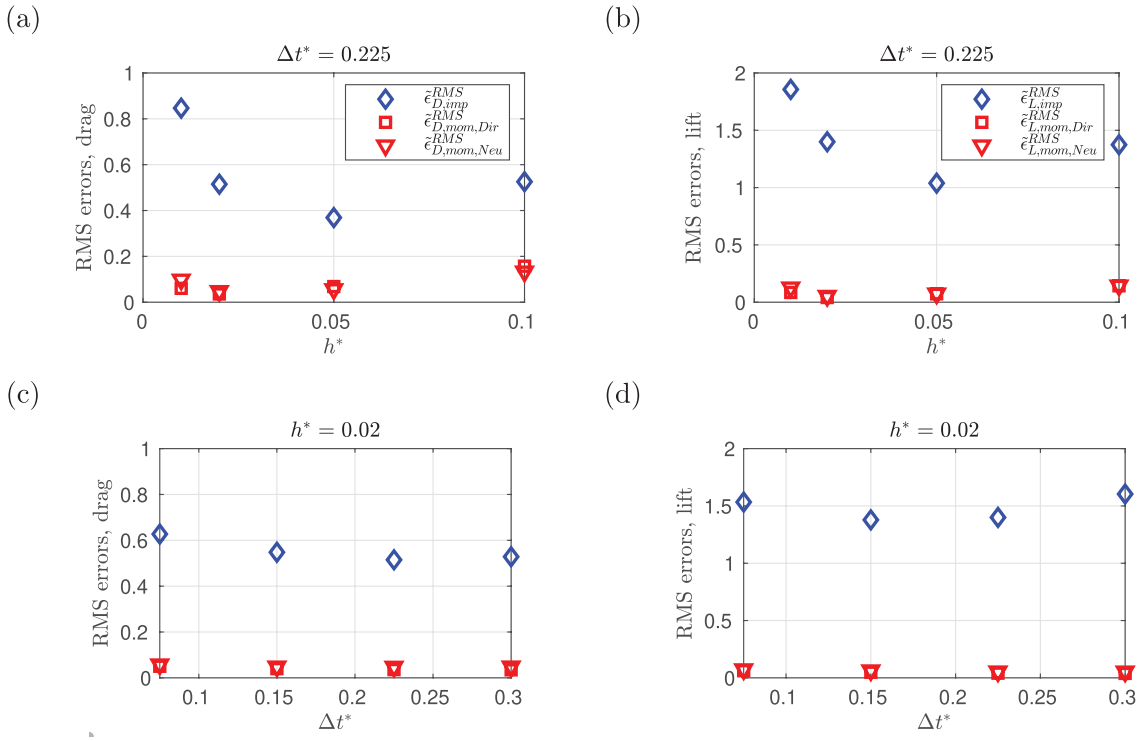

Figure 9. RMS errors in drag coefficients (left) and lift coefficients (right) with correlated random error added to the velocity fields: (a) and (b) variable h^*, constant $\Delta t^* = 0.225$; (c) and (d) variable Δt^*, constant $h^* = 0.02$.

shown in table 4. These values are calculated relative to the same terms evaluated without error, and normalized in the same manner as the force coefficients. The errors in the $\hat{n}u^2$ and $(\hat{n} \cdot \mathbf{u})\mathbf{u}$ components of the velocity term are anti-correlated, and their sum exhibits lower RMS error than the $(\hat{n} \cdot \mathbf{u})\mathbf{u}$ component alone. Combining the RMS errors of the four terms according to $\epsilon_{\text{comb}} = (1/4 \sum_{i=1}^{4} \epsilon_i^2)^{1/2}$ (as shown in the 'combined' row in table 4), it is similar to the RMS error in the total force (as shown in the 'total' row in table 4), indicating near independence of the random error contributions of the individual terms.

The viscous term's RMS error contribution is several times greater than its peak drag contribution. If only drag estimates were of interest, it might be advisable to neglect the viscous term when Reynolds number is of the order 10^3 or greater, reducing error propagation while introducing little systematic error. However, as shown in figure 6(d), the instantaneous lift contribution of the viscous term is of the same order as the lift amplitude, and thus it cannot be neglected unless a shift of origin is considered. Moving the origin to lie on the downtream plane, which would render the lift contribution of the viscous term zero, was done by Noca (1997) to yield

improved lift estimates. The velocity term is responsible for an order of magnitude less error propagation than the others. The impulse derivative and impulse flux terms are the most significant propagators of random error.

In cases where it is possible to identify a deforming control volume that avoids the wake vortices, as performed for the 'dynamic CV' cases above, random and systematic errors in the impulse method could be reduced. If one can identify a control surface on which $\boldsymbol{\omega} \approx 0$ and $\partial\boldsymbol{\omega}/\partial n \approx 0$, as suggested by Kang *et al* (2017), then equation (2) reduces to

$$\mathbf{F} = -\rho\frac{\mathrm{d}}{\mathrm{d}t}\int_V \mathbf{x}\times\boldsymbol{\omega}\mathrm{d}V + \rho\oint_S\left(\frac{1}{2}\hat{\mathbf{n}}u^2 - (\hat{\mathbf{n}}\cdot\mathbf{u})\mathbf{u}\right)\mathrm{d}S. \quad (4)$$

Note that the velocity term can be replaced by an integral of the Lamb vector, $\mathbf{u}\times\boldsymbol{\omega}$, to recover the formulation presented by Kang *et al* (2017). It remains for future work to determine whether such a substitution would have any effect on systematic or random errors when using typical experimental data. In either case, the simplification brought by a deformable CV definition eliminates errors associated with the cancellation of impulse and impulse-flux contributions, as discussed previously, and it eliminates the random error associated with the impulse flux and viscous terms, with the former being the largest single contributor. This simplification would reduce the total RMS error to near that of the impulse term alone. However, the drag and lift RMS errors in the impulse derivative in table 4 (0.357 and 0.692, respectively) are still significantly higher than the RMS errors for momentum-based methods for any spatial or temporal resolution in figure 9. In order to further reduce random error in the impulse-based force estimates, additional post-processing of the velocity field after the addition of synthetic random error needs to be considered.

Two common steps in the post-processing of PIV velocity fields are investigated to show their effect on random error propagation: (i) outlier detection and removal, and (ii) spatial filtering. The universal outlier technique of Westerweel and Scarano (2005) is employed; outliers are identified as those points whose velocities are not within 2.5 standard deviations of their eight closest neighbours, and are replaced by the mean of those same points. The resulting fields are then subject to Gaussian filters with window sizes ranging from 3×3 to 25×25. The window width, w, and standard deviation of the Gaussian curve, c, are related for all tested filters as $w = 4c/h^* + 1$. The corresponding range of normalized standard deviations is from $c/D = 0.01$ to 0.12. Figure 10(a) shows a snapshot of the normalized vorticity field with random error added at $t^* = 0$; figure 10(b) shows the vorticity field calculated after outlier removal and replacement and Gaussian filtering of the velocity fields, using $c/D = 0.03$ (over a 7×7 window). For this analysis, resolutions of $h^* = 0.02$ and $\Delta t^* = 0.075$ are used.

Figure 11 shows mean and RMS errors in estimated drag coefficients for a range of synthetic random error levels using the static-CV impulse method. As before, errors are calculated relative to the force estimates made in the absence of random velocity error, not relative to the CFD results. Maximum standard deviations of the shear-dependent synthetic error of $\sigma_{\text{flow}} = 0.019$, 0.038, and 0.075 were tested, and the corresponding standard deviations of the global synthetic error were $\sigma_{\text{global}} = 0.0013$, 0.0025 and 0.005. Recall that the values used in the generation of figures 8 and 9 were $\sigma_{\text{flow}} = 0.075$ and $\sigma_{\text{global}} = 0.005$. In this analysis, the mean drag bias is subtracted prior to calculating RMS error to decouple systematic and random errors. This differs from the error results reported in the conference paper upon which the present manuscript is based (Limacher *et al* 2019a), which are reproduced in figures 5 and 9, and in which the calculated RMS errors include contributions from bias errors and zero-mean random errors.

Table 4. Normalized RMS error contributions from each term in equation (2), calculated relative to their values in the absence of random velocity error. Resolutions were $h^* = 0.02$ and $\Delta t^* = 0.075$ for this analysis. The 'combined' row shows the RMS of the four contributions above it. The 'total' row represents the RMS error of the total force, as previously shown in figure 9. The similarity of the 'combined' and 'total' values indicates that the random errors in each term are nearly independent of one another.

Term /	RMS error	RMS error
	Drag	Lift
Impulse derivative	0.357	0.692
Impulse flux	0.411	1.165
Velocity term	0.019	0.020
Viscous term	0.200	0.366
Combined	0.580	1.404
Total	0.588	1.457

All four subplots of figure 11 demonstrate that the outlier detection and removal had a negligible effect on both the random and mean errors in lift and drag. As the Gaussian filter standard deviation is increased from $c/D = 0.03$ to 0.07 and 0.11, the RMS error decreases substantially in both lift and drag (figures 11(c) and (d)), but this comes at the cost of an increasing bias (underprediction) in the drag coefficient estimate (figure 11(a)). Figure 12 shows the force histories for these post-processing variants for the error level $\sigma_{\text{flow}} = 0.019$, demonstrating a decrease in random error for both lift and drag estimates, and the accompanying drag underprediction. The random error propagated to the final force histories appears to depend roughly linearly on the uncertainty in the velocity fields.

The systematic biases introduced by the Gaussian filter can be seen more clearly by considering velocity fields without random error added. Figure 13(a) and (b) show the calculated drag and lift coefficients using the static-CV impulse method (with $h^* = 0.02$ and $\Delta t^* = 0.075$) after application of Gaussian filters with a range of c/D. The increasing filter standard deviation blunts the lift peaks slightly, and yields a significant and increasing underprediction of drag. Figure 14 plots the calculated mean error in the drag estimates over the same range of c/D. Even modest filtering introduces a noticeable drag bias. The lowest two values of c/D in figure 14

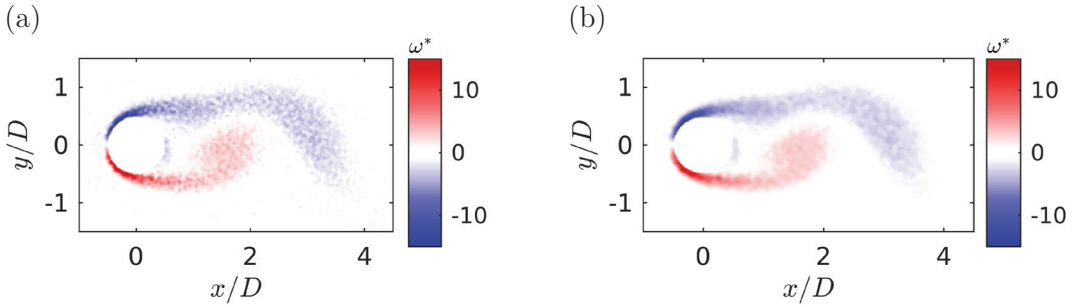

Figure 10. Snapshot of the normalized vorticity field at $t^* = 0$ calculated from velocity fields with a spatial resolution of $h^* = 0.02$ and with correlated random error added: (a) no post-processing; (b) after outlier removal and replacement and a Gaussian filter of standard deviation $c/D = 0.03$ applied over a 7×7 vector window.

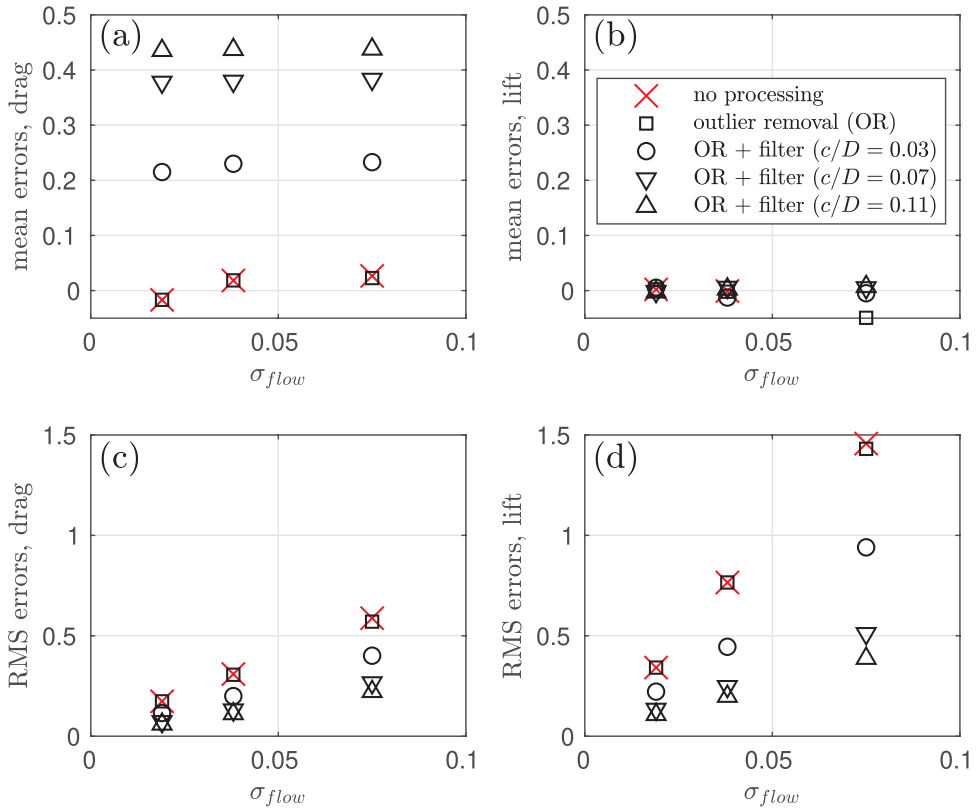

Figure 11. Mean (bias) error (a,b) and RMS errors after bias removal (c, d) in drag (a, c) and lift (b, d) coefficient for three levels of random error, represented by σ_{flow}, at various stages of post-processing: without post-processing (red X markers); after outlier detection and removal (squares); and after outlier detection/removal plus spatial Gaussian filters of varying standard deviation, c/D (circles, downward-pointing triangles, upward-pointing triangles).

correspond to the smallest possible filter windows of 3×3 and 5×5, but even these yield bias errors of about 3% and 11%, respectively, relative to the mean drag coefficient of 1.30 from the unaltered CFD results.

Other types of spatial filters have not been considered here, although the 'denoising filter' available in LaVision's DaVis software is briefly discussed in section 4.1. Since common filters are based on the limited subset of data in the neighbourhood of a given location, they are prone to attenuating local gradients, and thus the use of global data conditioning methods, such as proper orthogonal decomposition (POD) based filters (Raiola *et al* 2015), is of interest and should be explored in future studies.

4. Experimental investigation

4.1. Experimental methodology

The PIV dataset used in the present investigation is taken from the work of Limacher *et al* (2019b). A brief description of their methodology now follows, but the reader should refer to the original work for further details. The cylinder was towed through quiescent water with a triangular acceleration profile, with a peak dimensionless acceleration of $a_p^* = a_p D/U_{\max}^2 = 1$, where a_p is the peak instantaneous acceleration. One trial from the highest acceleration case ($a_p^* = 1.00$) of the original work is considered. The acceleration phase is complete at a

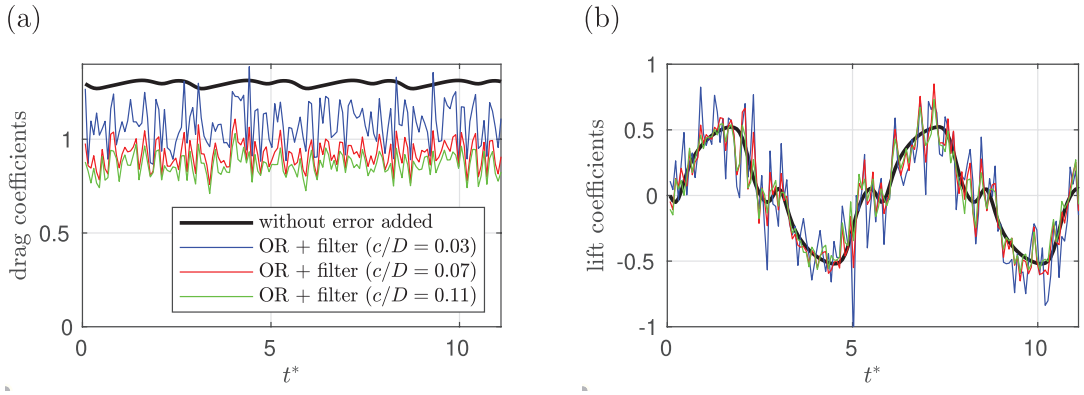

Figure 12. Calculated force coefficients versus t^* using the static-CV impulse method on velocity fields with no error added (thick black lines), and with error ($\sigma_{\text{flow}} = 0.019$, $\sigma_{\text{global}} = 0.0013$) and subsequent post-processing, including outlier detection/removal (OR) and the application of a Gaussian spatial filter with normalized standard deviations of $c/D = 0.03$ (blue lines), $c/D = 0.07$ (red lines), and $c/D = 0.11$ (green lines).

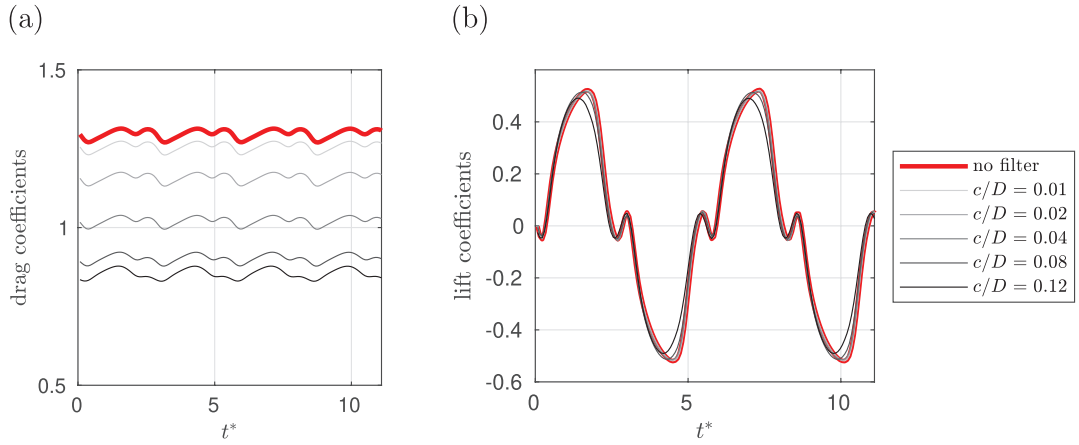

Figure 13. Calculated (a) drag coefficients and (b) lift coefficients using the static-CV impulse method on velocity fields without added random error, and with no filtering applied (red line) and after applying Gaussian filters of increasing normalized standard deviation, c/D (gray lines of increasing darkness).

dimensionless time of $t^* = tU_{\max}/D = 2.0$, where $U_{\max}$ is the maximum velocity attained, corresponding to a peak Reynolds number of approximately $\text{Re} = U_{\max}D/\nu = 5100$. The forces calculated using the two methods are compared to the direct measurements obtained using a six-axis force transducer (ATI Mini40) mounted above the waterline. Based on a static calibration, the uncertainty of the associated force measurements were estimated to be within 2% for the conditions investigated here. A dynamic calibration was also undertaken to remove the inertial bias experienced due to the acceleration of the device, as described at length in Limacher *et al* (2019b).

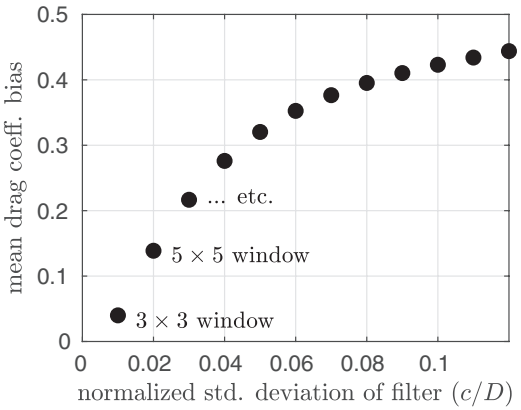

Figure 14. Mean bias (underprediction) in drag coefficient, calculated using the static-CV impulse method, versus normalized standard deviation (c/D) of the Gaussian filter applied to the velocity fields prior to force calculation. Each data point represents a two-vector increase in filter width from the data point to its left, giving window sizes of 3×3, 5×5, 7×7, etc.

4.2. Experimental results

Both force estimation methods utilize a control volume that is fixed relative to the cylinder. During the time interval investigated, no vorticity crosses the domain boundaries, allowing all of the contour integrals in the impulse formulation to be

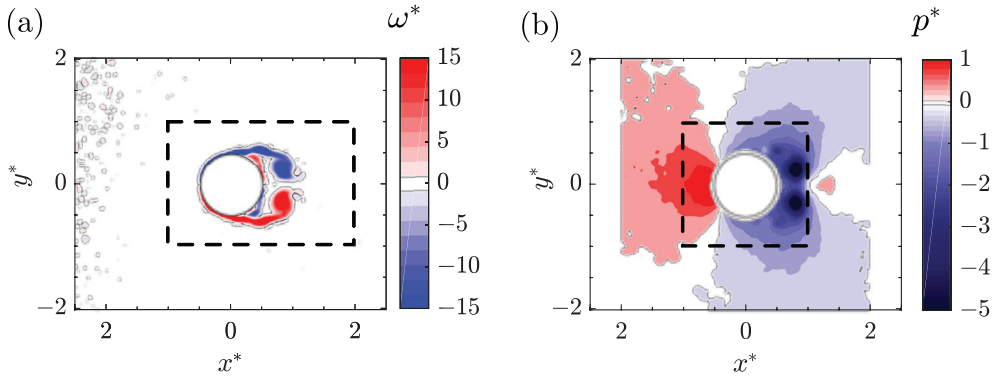

Figure 15. (a) Vorticity field with impulse formulation CV indicated with a black dashed line at $t^* = 3.5$ and (b) pressure field with momentum formulation CV indicated with a black dashed line at $t^* = 3.5$.

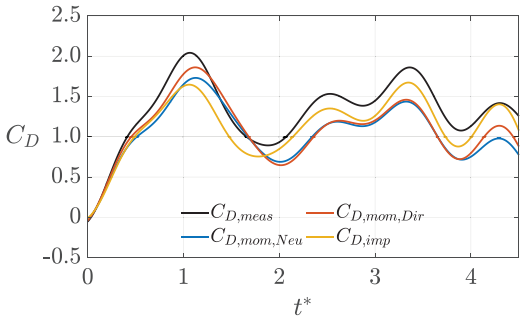

Figure 16. Comparison of filtered force estimates for the accelerating cylinder experiment with filtered force balance data ($C_{D,\mathrm{meas}}$).

omitted. The acceleration of the cylinder requires the addition of another term:

$$\mathbf{F} = -\rho \frac{\mathrm{d}}{\mathrm{d}t} \int_V \mathbf{x} \times \boldsymbol{\omega} \mathrm{d}V + \rho V_b \frac{\mathrm{d}u_c}{\mathrm{d}t}, \tag{5}$$

where $\mathrm{d}u_c/\mathrm{d}t$ is the cylinder acceleration, defined here to be positive, and V_b is the body volume (Limacher *et al* 2019b). This term is distinct from the classical added-mass force, since it lends a force in the *same* direction as the acceleration, not in opposition to it. Figure 15(a) shows an instantaneous vorticity field derived from the PIV measurements at $t^* = 3.5$ (during the constant-velocity translation phase), with the black dashed line denoting the boundary of the control volume used to compute impulse ($-1 < x^* < 2$, $-1 < y^* < 1$), while figure 15(b) shows an instantaneous pressure field computed from the Poisson equation with all Neumann boundary conditions, with the black dashed line denoting the boundary of the control volume used to compute the momentum balance ($-1 < x^* < 1$, $-1 < y^* < 1$). The Poisson equation is solved on a domain of $-2 < x^* < 2$, $-2 < y^* < 2$, and the Neumann boundary condition near the cylinder surface is applied on a larger circle of radius $r/D = 0.55$, in order to avoid boundary condition errors associated with computing temporal derivatives near the moving cylinder surface. Since the contribution of pressure to the momentum balance is only through integration along the outer contour of the CV (equation (1)), the force estimate is insensitive to position of the inner Poisson equation boundary condition.

The force estimations from the impulse and momentum formulations are compared to experimental force-balance data in figure 16. The compared data are low-pass filtered to remove frequencies associated with resonance vibrations of the model, which contaminate the transient measurements. The results of all methods produce signals that, once filtered, have high correspondence to the reference force balance measurements. The force estimates resolve the large initial peak in the force history during the cylinder's acceleration phase. Both methodologies underpredict the drag force slightly, but their fluctuations exhibit high temporal correlation. This underprediction is more pronounced for the momentum formulation at $t^* \geqslant 2$. This is attributed to the effect of finite spatial resolution on the Poisson pressure solution, resulting in an underprediction of pressure extremes in the stagnation region and low pressure wake vortices (de Kat and van Oudheusden 2012). For the impulse formulation, it was previously speculated that the finite resolution of the PIV data may lead to an underprediction of the viscous drag component associated with computing the vorticity near the cylinder surface (Limacher *et al* 2019b). However, it now seems plausible that the 5×5 'denoising filter' applied to the PIV velocity fields in the DaVis software is responsible for the bias error in the impulse-based drag estimate, given that a 5×5 Gaussian filter applied to the numerical data gave a drag underprediction of similar magnitude (see figure 14). Within the specified window, the denoising filter removes high-frequency noise by replacing velocity data with values interpolated on a second-order polynomial surface fitted through the original data (LaVision GmbH 2016).

5. Conclusions

A comparative analysis of momentum and impulse-based methods of force estimation using two-dimensional velocity data has been carried out. The comparison considered the effects of spatial resolution, temporal resolution and random velocity error. The methods were applied to two datasets: a numerical dataset of the flow around a stationary circular cylinder at $\mathrm{Re} = 150$, and a PIV dataset of the flow around a cylinder accelerating from rest in a quiescent fluid. Almost universally, the impulse method was shown to exhibit greater errors when applied to the flow over a stationary model.

The key exception is when using coarse spatial resolutions, for which an underestimation of drag is obtained using the momentum method. Addressing this shortcoming remains an important avenue for future work.

The impulse method also exhibits greater random-error sensitivity than the momentum method, which was established by artificially adding spatially correlated random error to the velocity fields. Caution is advised when using spatial filtering of the velocity fields to attenuate random errors, as even the use of relatively narrow-window Gaussian filters was shown to cause a notable understimation in the drag estimates using the impulse method. The investigation of other types of spatial filters, or other methods of random error mitigation, such as truncation of a proper orthogonal decomposition (POD) series, are suggested for future work.

If one is interested mainly in accurate force estimates, and interest in a specific mode of physical interpretation is secondary, then the presented momentum method is a more robust choice than the impulse method, at least when vorticity is expected to cross the domain boundaries. A key motivation for the continued study of impulse methods is the appealing possibility of attributing force components to the evolution of specific vortical structures. Fortunately, the present work suggests that efforts to identify CVs that enclose such structures are also likely to reduce error by avoiding vorticity on the bounding control surface. Particularly suitable problems for the impulse method include starting flows, such as the surging cylinder case considered herein using PIV data, or cyclic movements in an otherwise quiescent fluid. The momentum method, on the other hand, can be applied with greater confidence to problems with a non-zero freestream flow and an established wake, provided sufficient spatial resolution is obtained.

Acknowledgments

The authors acknowledge the Natural Sciences and Engineering Research Council of Canada (NSERC) for the funding of this work.

ORCID iDs

Eric Limacher https://orcid.org/0000-0002-1391-6208
Serhiy Yarusevych https://orcid.org/0000-0003-2723-2744
Chris Morton https://orcid.org/0000-0002-9991-5598

References

David L, Jardin T and Farcy A 2009 On the non-intrusive evaluation of fluid forces with the momentum equation approach *Meas. Sci. Technol.* **20** 095401

de Kat R and van Oudheusden B 2012 Instantaneous planar pressure determination from PIV in turbulent flow *Exp. Fluids* **52** 1089–106

Henderson R D 1995 Details of the drag curve near the onset of vortex shedding *Phys. Fluids* **7** 2102–4

Kang L, Liu L, Su W and Wu J 2017 A minimum-domain impulse theory for unsteady aerodynamic force with discrete wake *Theor. Appl. Mech. Lett.* **7** 306–10

LaVision GmbH 2016 FlowMaster product-manual for DaVis 8.3

Limacher E, McClure J, Yarusevych S and Morton C 2019a Comparison of momentum and impulse methods of force estimation using PIV data *13th Int. Symp. on Particle Image Velocimetry—ISPIV2019 (Munich, Germany, 22–4 July 2019)*

Limacher E, Morton C and Wood D 2019b On the calculation of force from PIV data using the generalized added-mass and circulatory force decomposition *Exp. Fluids* **60** 4

Lin J-C and Rockwell D 1996 Force identification by vorticity fields: techniques based on flow imaging *J. Fluids Struct.* **10** 663–8

Marzouk O, Nayfeh A H, Akhtar I and Arafat H N 2007 Modeling steady-state and transient forces on a cylinder *J. Vib. Control* **13** 1065–91

McClure J and Yarusevych S 2017a Optimization of planar PIV-based pressure estimates in laminar and turbulent wakes *Exp. Fluids* **58** 62

McClure J and Yarusevych S 2017b Instantaneous PIV/PTV-based pressure gradient estimation: a framework for error analysis and correction *Exp. Fluids* **58** 92

McClure J, Morton C and Yarusevych S 2015 Flow development and structural loading on dual step cylinders in laminar shedding regime *Phys. Fluids* **27** 063602

McClure J and Yarusevych S 2019 Planar momentum balance in three-dimensionalows: applications to load estimation *Exp. Fluids* **60** 41

Mohebbian A and Rival D E 2012 Assessment of the derivative-moment transformation method for unsteady-load estimation *Exp. Fluids* **53** 319–30

Morton C and Yarusevych S 2010 Vortex shedding in the wake of a step cylinder *Phys. Fluids* **22** 083602

Noca F 1997 On the evaluation of time-dependent fluid-dynamic forces on bluff bodies *PhD Thesis* California Institute of Technology

Noca F, Shiels D and Jeon D 1999 A comparison of methods for evaluating time-dependent fluid dynamic forces on bodies, using only velocity fields and their derivatives *J. Fluids Struct.* **13** 551–78

Norberg C 2003 Fluctuating lift on a circular cylinder: review and new measurements *J. Fluids Struct.* **17** 57–96

Pan Z, Whitehead J, Thompson S and Truscott T 2016 Error propagation dynamics of PIV-based pressure field calculations: how well does the pressure Poisson solver perform inherently? *Meas. Sci. Technol.* **27** 084012

Raiola M, Discetti S and Ianiro A 2015 On PIV random error minimization with optimal POD-based low-order reconstruction *Exp. Fluids* **56** 75

Rival D E and van Oudheusden B 2017 Load-estimation techniques for unsteady incompressible flows *Exp. Fluids* **58** 20

Sciacchitano A and Wieneke B 2016 PIV uncertainty propagation *Meas. Sci. Technol.* **27** 084006

van Oudheusden B 2013 PIV-based pressure measurement *Meas. Sci. Technol.* **24** 032001

Van Oudheusden B W, Scarano F and Casimiri E W F 2006 Non-intrusive load characterization of an airfoil using PIV *Exp. Fluids* **40** 988–92

Versteeg H K and Malalasekera W 2007 *An Introduction to Computational Fluid Dynamics: the Finite Volume Method* 2nd edn (New York: Pearson Education Limited)

Westerweel J and Scarano F 2005 Universal outlier detection for PIV data *Exp. Fluids* **39** 1096–100

Wieselberger C 1921 New data on the law of hydro and aerodynamics resistance *Phys. Z.* **22** 321–8

Wu J Z, Ma H Y and Zhou M D 2015 *Vortical Flows* (Berlin: Springer)